J Mater Sci (2008) 43:6359–6365
DOI 10.1007/s10853-008-2900-y

Facile synthesis of ordered mesoporous silica with high γ-Fe_2O_3 loading via sol-gel process

Jiansheng Li · Y. S. Lin

Received: 13 June 2008 / Accepted: 22 July 2008 / Published online: 16 August 2008

Abstract A series of ordered mesoporous silica loaded with iron oxide was synthesized by facile one-step sol-gel route using Pluronic P123 as the template, tetraethylorthosilicate as the silica source, and hydrated iron nitrite as the precursor under acid conditions. The as-synthesized materials with Fe/Si molar ratio ranging from 0.1 to 0.8 were characterized by X-ray diffraction (XRD), transmission electron microscopy (TEM), vibrating sample magnetometry (VSM), and N_2 adsorption porosimetry. All samples possess ordered hexagonal mesoporous structure similar to SBA-15, with a high surface area, large pore volume, and uniform pore size. Although higher iron content causes a distortion of hexagonal ordering structure to some extent, the materials still maintain the ordered mesopore structure even with Fe/Si molar ratio as high as 0.8. Pore structure and TEM data suggest that iron oxide nanoparticles are buried within the silica wall, and increasing the iron oxide loading has little effects on the pore structure of the mesoporous silica. VSM results show as-synthesized samples exhibit superparamagnetic behavior.

Introduction

Nanosized γ-Fe_2O_3(maghemite) has been found to possess unique magnetic, catalytic, optical, sorption, and other properties, enabling its functionalization in many advanced nanotechnological applications such as in information-storage media [1], catalysis [2], magnetic fluids [3], magneto-optical devices [4], image-intensifying agent for nuclear magnetic resonance imaging [5], and other medical uses [6–8]. Synthesis of iron oxide nanoparticles has gained considerable attention in the past decades. The challenges for synthesis of pure nanosized γ-Fe_2O_3 partially are due to the fact that γ-Fe_2O_3 (maghemite) can easily transform to α-Fe_2O_3 (hematite) at high temperatures. Moreover, γ-Fe_2O_3 nanoparticles tend to aggregate resulting in an increase in the particle size which facilitates the γ-to-α transition [9]. Applying ceramic coating or encapsulating magnetic nanoparticles within silica matrix has been demonstrated effective in preventing aggregation and stabilizing the maghemite phase. For dispersing nanosized γ-Fe_2O_3 particles in nonmetallic matrices, sol-gel methods are commonly used. This method includes mixing of tetrathoxysilane and ferric salt (nitrate, chloride) alcoholic solutions, followed by the thermal treatment of the gel [10–12]. The presence of the silica coating can effectively protect the iron oxide nanoparticles from aggregation at sintering temperatures up to 1000 °C [13].

The discovery of mesoporous silica templated by surfactant has sparked much interest in the incorporation of iron oxide particles into ordered silica matrices. In general, there are three major methods for synthesis of iron-containing mesoporous silica. The most common method is the post-synthesis impregnation of the preformed porous material such as MCM-41 [14], MCM-48 [15], SBA-15 [16] with an inorganic precursor like $Fe(NO_3)_3$ and conversion to oxide by calcination. But this post-synthesis method requires more synthesis and characterization steps and suffers from the problem that iron oxide particles clog the pore structure and form agglomerates outside the mesopores. The second

J. Li · Y. S. Lin (✉)
Department of Chemical Engineering, Arizona State University, Tempe, AZ 85287-6006, USA
e-mail: Jerry.Lin@ASU.edu

J. Li
Department of Environmental Science & Engineering, Nanjing University of Science and Technology, Nanjing 210094, China

approach to synthesize iron-containing mesoporous materials is hydrothermal method, which has been used in synthesis of Fe-MCM-41 [17, 18], Fe-MCM-48 [19], Fe-SBA-15 [20], Fe-TUD-1 [21], Fe-MFS-9 [22]. However, with the hydrothermal method it is difficult to control precisely the stoichiometric composition of resultant materials due to inevitable existence of residual metal ion in synthesis solution.

The third method, known as sol-gel route, is a more promising method to obtain nanosized metal oxide in ordered mesoporous silica matrix. In the direct synthesis process, silica and iron oxide precursors are mixed in solution and condensed by sol-gel processing to form a mixed metal oxide network. The higher hydrolysis and condensation rate of iron precursor that would result in precipitation of iron oxide before the sol-gel process of the siliceous species starts, has been overcome by pre-hydrolysis of the silica sol [23] or modification of surfactant method [24, 25]. Recently, Yang et al. [26] developed more simple one-step route for synthesis of highly ordered mesoporous silica monoliths with various metal oxide nanocrystals, including those of Cr_2O_3, MnO, Fe_2O_3, Co_3O_4, NiO, CuO, ZnO, CdO, SnO_2, and In_2O_3. However, the dispersion of γ-Fe_2O_3 in silica matrix was not detailed and the molar ratio of Fe/Si was only up to 0.2. In this present work, we studied synthesis of ordered mesoporous silica with higher iron oxide loading by the sol-gel method, and investigated the nature and local environment of iron species in mesoporous silica matrix and its effect on pore structure and magnetic properties. The objective of this paper is to report the synthesis and properties of the mesoporous silica with higher iron oxide loading.

Experimental section

Material synthesis

The procedure for synthesis of pure silica and iron-containing silica was based on the work of Yang et al. [26] with some modifications. The typical synthesis procedure is as follows: 1.4 g Pluronic P123 (P123, $EO_{20}PO_{70}EO_{20}$, $M_{av} = 5800$, BASF) was added to 2.8 g tetraethylorthosilicate (TEOS, Aldrich). It was stirred at 60 °C for 10 min till the P123 was dissolved completely and the mixture of P123 and TEOS was obtained. Hydrated iron nitrite ($Fe(NO_3)_3 \cdot 9H_2O$, Aldrich) in an amount corresponding to Fe/Si molar ratio of 0.1, 0.2, 0.3, 0.4, 0.5, 0.6, 0.7, and 0.8 was dissolved in 18.0 g of ethanol. The obtained solution (or 18.0 g ethanol for pure silica sample) was subsequently added to the mixture of P123 and TEOS and stirred for further 10 min at 60 °C. Then it was cooled to room temperature, and 1.0 mL aqueous HCl (0.05 mol L^{-1}) was added to the solution and stirred for further 2.0 h. After 24 h aging, the sols were poured into petri dishes and dried in air at 25 °C and relative humidity of 80% in a humidity controlled oven. After 48 h evaporation, the sols turned to wet gels. The wet gels were dried at 105 °C for 12 h and then heat-treated at 400 °C for 4 h (at a ramping rate of 0.5 °C min^{-1}). The resultant samples are denoted as S0, S0.1, S0.2, S0.3, S0.4, S0.5, S0.6, S0.7, and S0.8, in which the arithmetic labels denote the molar ratio of iron to silicon.

Characterization

The samples after calcination were ground into powders for characterization. X-ray diffraction (XRD) patterns were obtained on a Bruker D8 diffractometer using Cu Kα radiation with the step size of 0.02°/s at 40 kV and 40 mA. The magnetic properties of iron-containing samples were measured using a Lakeshore LS307-930 vibrating sample magnetometry (VSM) magnetometer at room temperature. Hysteresis loops were obtained after applying a saturating field of 10,000 Oe. Transmission electron microscopy (TEM) bright-field (BF) and dark-field (DF) images, high-resolution TEM bright-field (BF) images, and selected-area electron diffraction (SAED) patterns were obtained on a JEOL JEM-2100 microscope, operating at 200 kV. For TEM measurements, the samples were prepared by dispersing the powdered products as slurry in ethanol, after which they were dispersed and dried on a holey carbon film on a copper grid. N_2 adsorption–desorption isotherms were measured using Micromeritics ASAP-2020 at liquid nitrogen temperature (77 K). The specific surface areas were evaluated using the Brunauer-Emmett-Teller (BET) method.

Results and discussion

Material structure properties

Figure 1 shows low-angle XRD (LAXRD) patterns of mesoporous silica with various iron contents. For pure silica sample, S0, it exhibits a sharp diffraction peak at 2θ of 1.11° and two weak peaks at 2θ of 1.92° and 2.18°, suggesting that the sample is in good long-range order. These peaks can be indexed as diffractions from (100), (110), and (200) planes of the hexagonal space group (p6 mm). This XRD diffraction pattern is in agreement with that for SBA-15 [27]. After introduction of iron species to silica matrix, the observed diffraction peaks shift to lower angle direction. The unit cell parameter $a = 2d_{100}/\sqrt{3}$ is increased from 9.18 nm for pure silica to 9.62–9.99 nm for iron-containing samples. The (100) peak

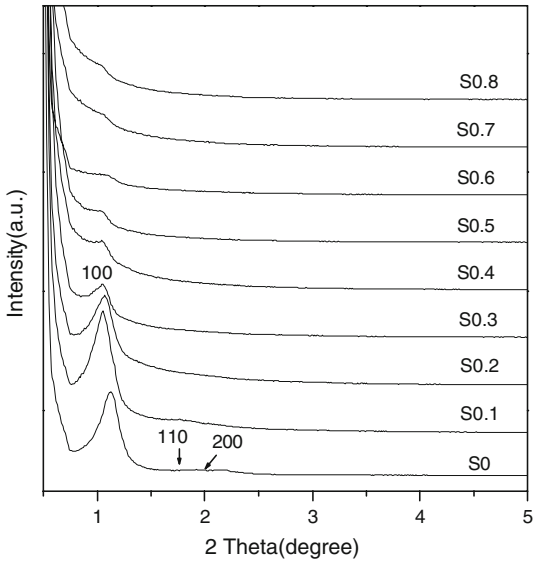

Fig. 1 Low-angle XRD patterns of mesoporous silica with various iron contents

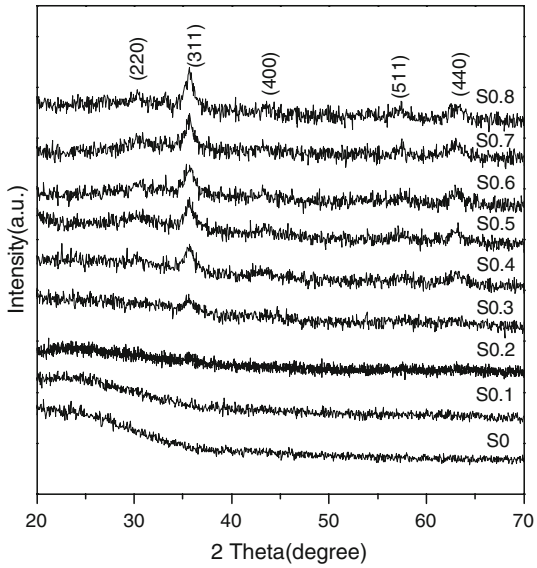

Fig. 2 Wide-angle XRD patterns of mesoporous silica with various iron contents

can be found in all samples suggesting that the ordered mesoporous structure can be maintained after introduction of different amounts of iron species. However, when the molar ratio of Fe/Si is higher than 0.2, (110) and (200) peaks disappear and only (100) peak can be detected, and its intensity decreases gradually with increasing iron content. This is a clear indication that although the ordered mesoporous structure is retained at the Fe/Si molar ratio up to 0.8, higher iron content causes a distortion of hexagonal ordering structure to some extent.

In wide-angle XRD patterns (Fig. 2), no distinct diffraction peaks can be found in the sample with Fe/Si molar ratios lower than 0.2, i.e. S0 and S0.1, indicating that iron species in mesoporous silica matrix presents as amorphous Fe_2O_3 or ultrasmall nanocrystalline [28]. A very weak diffraction peak at 35.8° can be found in S0.2 (Fe/Si = 0.2). This peak can be indexed to (311) diffraction of γ-Fe_2O_3 (maghemite, JCPDS card no. 00-039-1346) [29]. For samples with Fe/Si higher than 0.2, the intensity of (311) diffraction peak increases gradually with increasing iron content and more diffraction peaks corresponding to γ-Fe_2O_3 are visible. For samples with Fe/Si molar ratios higher than 0.4, five well-resolved diffraction peaks at 30.3°, 35.8°, 43.4°, 57.4°, and 63.0° are observed. These peaks can be indexed to the (220), (311), (400), (511), and (440) diffraction for γ-Fe_2O_3 with a cubic structure [30], which is in agreement with the selected area electron diffraction (SAED) analysis (see below). Moreover, it can be also found that these diffraction peaks are obviously broadened, which suggests that iron species is present as very finely divided γ-Fe_2O_3 nanocrystals and no large particles are formed. Based on the half-height of the (311) diffraction peak of γ-Fe_2O_3, the average particle size of γ-Fe_2O_3 in S0.3–S0.8 samples is about 4.3, 4.8, 4.9, 5.2, 6.5, and 7.8 nm, respectively, estimated from the Scherrer equation [31].

Figure 3 shows representative TEM bright field images of mesoporous silica samples of different iron content. For samples with Fe/Si ratio lower than 0.5, TEM images show large domains with ordered, strip-like channels in characteristic [001] direction of the hexagonal mesostructure (similar to SBA-15 structure). For samples with higher Fe/Si ratio, i.e. S0.6, S0.7, and S0.8, the ordered hexagonal structure can still be observed. However, the hexagonal ordering decreases as the Fe amount incorporated into the silica walls increases. Clearly incorporation of higher amount of iron oxide in the silica distorts the ordered structure. As estimated directly from these TEM images, the distance between the neighboring channels in all iron-containing samples is about 9.5 nm, which is in agreement with the LAXRD results (Fig. 1).

In order to further understand the state of iron oxide nanoparticles in mesoporous silica, a detailed TEM analysis was performed. Typical TEM BF image and the corresponding SAED pattern, DF image, HRTEM image of sample S0.4 are shown in Fig. 4. The crystalline nature of iron oxide is evidenced by the SAED pattern and dark field image (Fig. 4b, c). There are five diffraction rings in the corresponding SAED pattern (Fig. 4b). These rings can be indexed to (220), (311), (400), (511), and (440) crystal planes of γ-Fe_2O_3, which is in good agreement with the XRD results (Fig. 2). The dark field image exhibits homogeneous dispersion of isolated γ-Fe_2O_3 nanoparticles over silica matrix. It is concluded that the synthesis

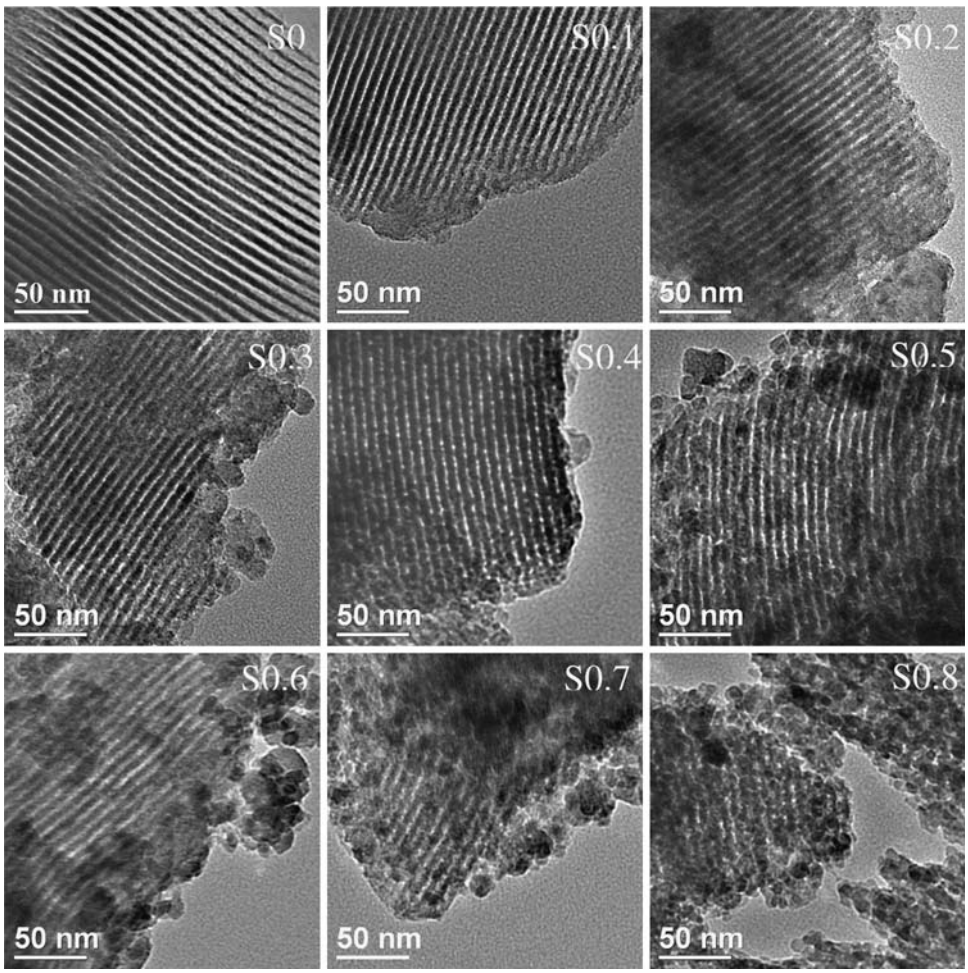

Fig. 3 TEM bright field images of mesoporous silica with various iron contents calcined at 400 °C for 4 h

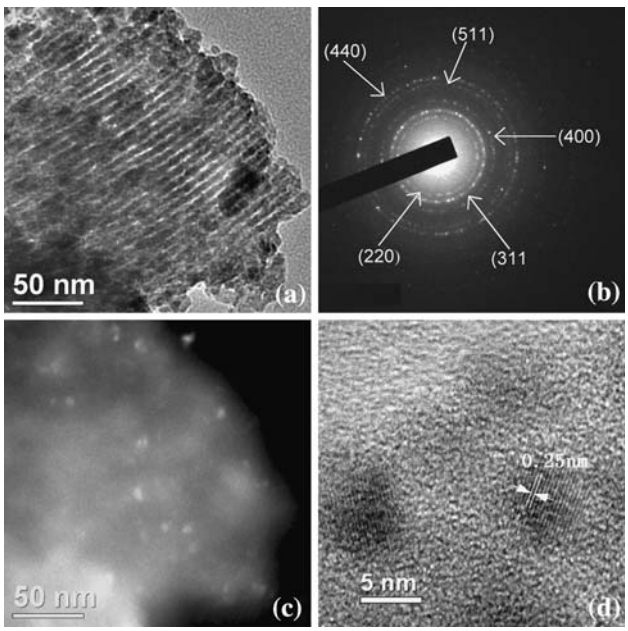

Fig. 4 (**a**) TEM bright field image, (**b**) the corresponding SAED pattern, (**c**) the corresponding TEM dark field image, and (**d**) high-resolution TEM bright field image of sample S0.4

procedure and the consecutive thermal treatment did not damage the ordered structure.

The diameter of the γ-Fe_2O_3 particles is estimated from TEM images at between 4.5 nm and 5.6 nm, close to the value calculated from Scherrer's equation. The HRTEM image shown in Fig. 4d illustrates that some of the nanocrystals can be separated out from the silica matrix and they are single crystal in nature. The lattice plane distance is 0.25 nm, which matches the (311) plane of γ-Fe_2O_3 [32]. It can be concluded that iron oxide is present as highly dispersed γ-Fe_2O_3 nanocrystals in the well-ordered hexagonal matrix.

Pore structural and magnetic properties

Figure 5 shows the nitrogen adsorption–desorption isotherms of mesoporous silica samples with different amounts of iron oxide. All isotherms are of typical Type IV model with a H1 hysteresis loop representative of mesopores [33]. The sharp inflections between the relative pressures $p/p_0 = 0.4$–0.7 in these isotherms correspond to capillary condensation within uniform mesopores. The

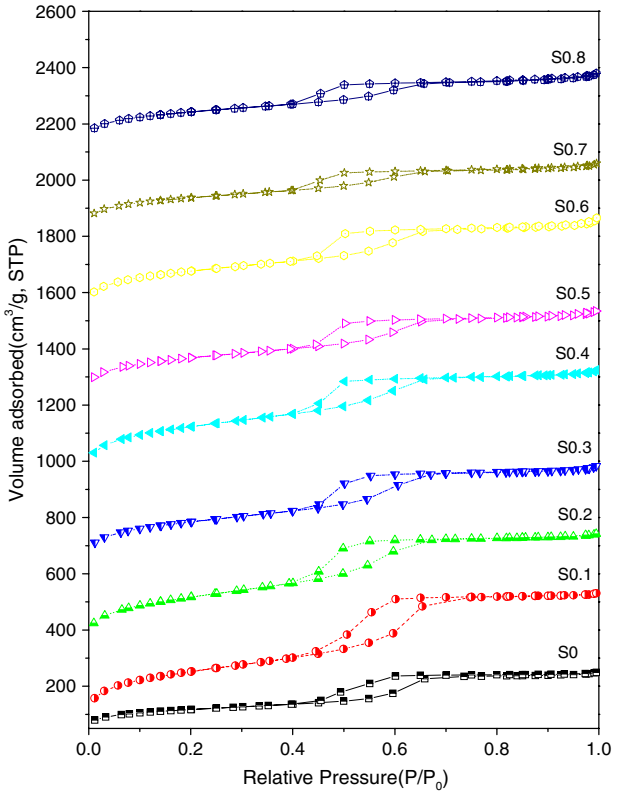

Fig. 5 Nitrogen adsorption–desorption isotherms of mesoporous silica with various iron contents. The isotherms of S0.2, S0.3, S0.4, S0.5, S0.6, S0.7, and S0.8 are offset by 300, 600, 900, 1200, 1500, 1800, and 2100 cm^3/g, respectively

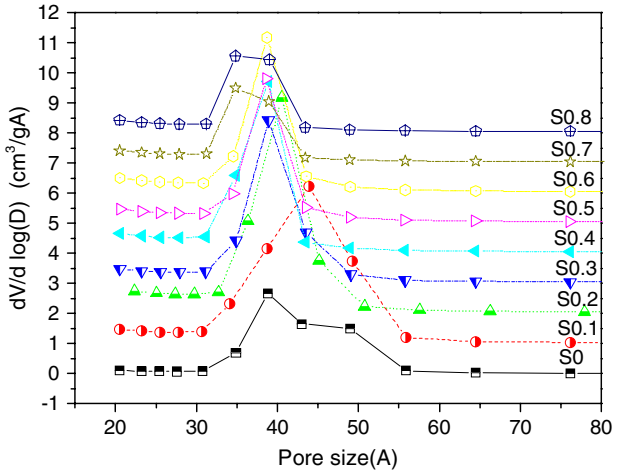

Fig. 6 Pore size distribution (PSD) of mesoporous silica with various iron contents. The pore size distribution of S0.1, S0.2, S0.3, S0.4, S0.5, S0.6, S0.7, and S0.8 are offset by 1, 2, 3, 4, 5, 6, 7, and 8 cm^3/g Å, respectively

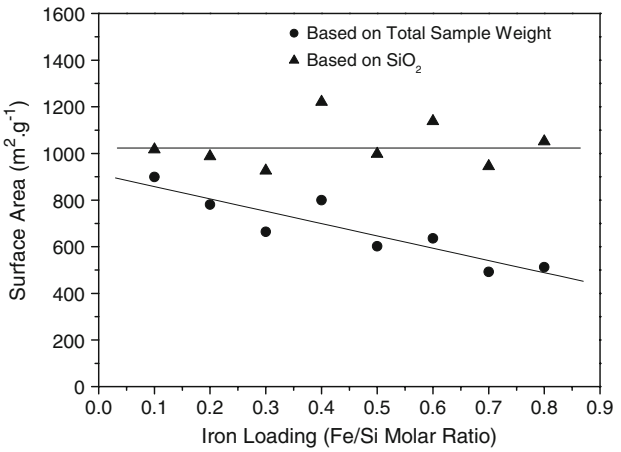

Fig. 7 Surface area of iron-doped silica sample based on the total weight and weight of silica

sharpness of this step demonstrates the uniform pore size distribution in these mesoporous materials. The sharpness of the inflection step and the amount of adsorbed nitrogen decrease gradually with increasing iron content. Also, the inflection positions on desorption branches shift slightly toward lower relative pressure with higher percentages of iron oxide loading.

Pore size distribution of all samples derived from the desorption branch are given in Fig. 6, where D denotes pore diameter. All samples exhibit a unimodal mesoporous size distribution, with an average pore size decreased slightly with increasing iron loading. These indicate that ordered mesopore structure still maintains after introduction of high iron content for these samples. The surface area of the iron-doped silica samples is shown in Fig. 7. Based on the total weight of the sample, the surface area decreases with increasing loading. However, the surface area, if based on the weight of silica, remains essentially constant with increasing iron loading, as shown in Fig. 7. This suggests that the presence of iron nanoparticles does not contribute to the surface area. One possibility is that iron oxide is buried within the silica, rendering its surface inaccessible by nitrogen. The doped silica samples have a surface area around 1000 m^2/g of SiO_2, much larger than the undoped silica sample (surface area of 411 m^2/g). In synthesizing iron-doped samples addition of nitrate iron lowered the pH of the synthesis solution, favoring formation of mesoporous silica with possibly microporous silica pore wall [34, 35]. This would give a larger surface area for the iron-doped silica.

The average pore diameter measured from nitrogen desorption isotherm and unit cell parameter from XRD data for the undoped and iron-doped silica samples are given in Table 1. The pore wall thickness can be calculated from these two sets of data and are also given in the table. As shown, the iron-doped silica samples have a smaller pore size, larger lattice parameter, and larger wall thickness as compared to the nondoped silica sample. There is no clear

Table 1 Pore structure parameters of samples measured by the adsorption branch of N_2 adsorption–desorption isotherms and LAXRD patterns

Sample ID	Molar ratio of Fe/Si	Average pore diameter d (nm)	Unit cell parameter a_0 (nm)	Pore wall thickness w (nm)
S0	0	4.2	9.2	5.0
S0.1	0.1	4.0	9.7	5.7
S0.2	0.2	3.8	9.6	5.8
S0.3	0.3	3.8	9.8	6.0
S0.4	0.4	3.6	9.8	6.2
S0.5	0.5	3.8	10.0	6.2
S0.6	0.6	3.9	9.8	5.9
S0.7	0.7	3.7	9.9	6.2
S0.8	0.8	3.8	9.9	6.2

Pore wall thickness w = Unit cell parameter a_0 − Average pore diameter d

iron content dependence of these three parameters for the iron-doped samples. These results suggest that iron oxide crystallite particles are present in silica wall and the pore (and wall) structure is not affected by the quantity of the iron oxide crystals in the pore wall. This difference in the pore and wall structure between the iron-doped silica samples and undoped sample is more likely due to the difference on the conditions for the sol-gel process due to the addition of iron nitrate in synthesis. This is consistent with the results on the surface area for the iron-doped and undoped silica samples.

Magnetic hysteresis measurements for all samples of mesoporous silica with different iron content calcined at 400 °C for 4 h were carried out in an applied magnetic field at room temperature (Fig. 8). The absence of room-temperature hysteresis in the magnetization curves indicated that the iron oxide particles in mesoporous silica matrix are superparamagnetic [36]. The saturation magnetization of obtained nanocomposites increases with increasing amount of γ-Fe_2O_3 in the silica matrix. The greatest value of saturation magnetization (16.7 emu/g), obtained for S0.8, is much smaller compared with the γ-Fe_2O_3 bulk material (82 emu/g) [37]. This may be due to the presence of nonmagnetic silica matrix on the sample and nanometric scale of γ-Fe_2O_3 particles embedded in mesoporous silica matrix.

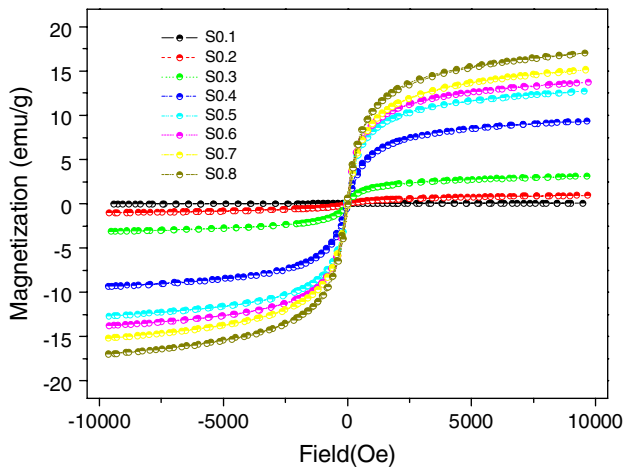

Fig. 8 Magnetization curves of mesoporous silica with various iron contents calcined at 400 °C for 4 h

Conclusions

In summary, a series of ordered mesoporous silica samples with different iron oxide loading was successfully synthesized via a one-step sol-gel route. All samples possess ordered hexagonal mesoporous structure similar to SBA-15 with high surface area, large pore volume, and uniform pore size. Increasing iron oxide loading causes distortion of the hexagonal ordering to some extent. The doped silica still maintains ordered mesoporous structure even with Fe/Si molar ratio as high as 0.8. Iron oxide is present as highly dispersed γ-Fe_2O_3 nanocrystals within the hexagonal silica walls. Increasing iron oxide loading has little effect on mesopore structure and silica surface area of the doped silica samples. The as-synthesized materials exhibit superparamagnetic behavior. The one-step sol-gel route is an effective and simple method for templating synthesis of ordered mesoporous γ-Fe_2O_3/SiO_2 composites.

Acknowledgements This work was supported by Petroleum Research Fund (Administered by the American Chemical Society), Natural Science Foundation of Jiangsu Province (grant no.BK2006205), and Young Scholar Science Foundation of Nanjing University of Science & Technology (grant no.NJUST 200502). JSL is grateful to China Scholarship Council for a fellowship to support his visit to ASU.

References

1. Ensling J, Gütlich P, Klinger R, Meisel W, Jachow H, Schwab H (1998) Hyperfine Interact 111:143. doi:10.1023/A:1012624827290
2. Zhu Q, Teeffelen R, Santen R, Hesen E (2004) J Catal 221:575. doi:10.1016/j.jcat.2003.09.025
3. Depeyrot J, Sousa EC, Aquino R, Tourinho FA, Dubois E, Bacri JC et al (2000) J Magn Magn Mater 252:375. doi:10.1016/S0304-8853(02)00623-6
4. Zayat MZ, del Monte F, Morales MD, Rosa G, Guerrero H, Serna CJ et al (2003) Adv Mater 15:1809. doi:10.1002/adma.200305436
5. Stroh A, Zimmer C, Gutzeit C, Jakstadt M, Marschinke F, Jung T et al (2004) Free Radic Biol Med 36:976. doi:10.1016/j.freeradbiomed.2004.01.016
6. McMichael RD, Schull RD, Swartzendruber LJ, Bennett LH, Watson RE (1992) J Magn Magn Mater 111:29. doi:10.1016/0304-8853(92)91049-Y
7. Josephson L, Tsung CH, Moore A, Weissleder R (1999) Bioconjug Chem 10:186. doi:10.1021/bc980125h

8. Nagano H, Machida Y, Iwata M, Imada T, Noguchi Y, Matsumoto A et al (1997) Int J Pharm 147:119. doi:10.1016/S0378-5173(96)04804-1
9. Ayyub P, Multani M, Barma M, Polkar VR, Vijayaraghavan R (1988) J Phys C Solid State Phys 21:2229. doi:10.1088/0022-3719/21/11/014
10. Niznansky D (1997) J Sol-gel Sci Tech (Paris) 8:615
11. Ennas G, Musinu A, Piccaluga G, Zedda D (1998) Chem Mater 10:495. doi:10.1021/cm970400u
12. Jitianu A, Crisan M, Meghea A, Rau I, Zaharescu M (2002) J Mater Chem 12:1401. doi:10.1039/b110652j
13. Zheng T, Pang J, Tan G, He J, McPherson GL, Lu Y et al (2007) Langmuir 23:5143. doi:10.1021/la063761+
14. Wingen A, Anastasievic N, Hollnagel A, Werner D, Schüth F (2000) J Catal 193:248. doi:10.1006/jcat.2000.2896
15. Fröba M, Köhn R, Bouffaud G (1999) Chem Mater 11:2858. doi:10.1021/cm991048i
16. Tsoncheva T, Rosenholm J, Teixeira CV, Dimitrov M, Linden M, Minchev C (2006) Microporous Mesoporous Mater 89:209. doi:10.1016/j.micromeso.2005.10.028
17. Wang Y, Zhang Q, Shishido T, Takehira K (2002) J Catal 209:186. doi:10.1006/jcat.2002.3607
18. Lu Y, Zheng J, Liu J, Mu J (2007) Microporous Mesoporous Mater 106:28. doi:10.1016/j.micromeso.2007.02.017
19. Shao Y, Wang L, Zhang J, Anpo M (2006) J Photochem Photobiol A 180:59. doi:10.1016/j.jphotochem.2005.09.018
20. Li Y, Feng Z, Lian Y, Sun K, Zhang L, Jia G et al (2005) Microporous Mesoporous Mater 84:41. doi:10.1016/j.micromeso.2005.05.021
21. Hamdy MS, Mul G, Jansen JC, Ebaid A, Shan Z, Overweg AR et al (2005) Catal Today 100:255. doi:10.1016/j.cattod.2004.10.018
22. Han Y, Meng X, Guan H, Yu Y, Zhao L, Xu X et al (2003) Microporous Mesoporous Mater 57:191. doi:10.1016/S1387-1811(02)00590-5
23. Garcia C, Zhang Y, Disalvo F, Wiesner U (2003) Angew Chem Int Ed 42:1526. doi:10.1002/anie.200250618
24. Huesing N, Launay B, Kickelbick G, Gross S, Armelao L, Bottaro G et al (2003) Appl Catal A 254:297. doi:10.1016/S0926-860X(03)00475-7
25. Supplit R, Hüsing N, Bertagnolli H, Bauer M, Kessler V, Seisenbaeva GA, Gross S et al (2006) J Mater Chem 16:4443. doi:10.1039/b606386a
26. Yang H, Lu Q, Gao F, Shi Q, Yan Y, Zhang F et al (2005) Adv Funct Mater 15:1377. doi:10.1002/adfm.200500026
27. Zhao D, Feng J, Huo Q, Melosh N, Fredrickson GH, Chmelka BF et al (1998) Science 279:548. doi:10.1126/science.279.5350.548
28. Machala L, Zboril R, Gedanken A (2007) J Phys Chem B 111:4003. doi:10.1021/jp064992s
29. Delahaye E, Escax V, El Hassan N, Davidson A, Aquino R, Dupuis V et al (2006) J Phys Chem B 110:26001. doi:10.1021/jp0647075
30. Hodgkins RP, Ahniyaz A, Parekh K, Belova LM, Bergström L (2007) Langmuir 23:8838. doi:10.1021/la063395u
31. Warren BE (1969) X-ray diffraction. Dover Publications, New York
32. Jing Z (2006) Mater Sci Eng A 441:176. doi:10.1016/j.msea.2006.08.013
33. Sing KSW, Everett DH, Haul RAW, Moscow L, Pierotti RA, Rouquerol J et al (1985) Pure Appl Chem 57:603. doi:10.1351/pac198557040603
34. Fotou GP, Lin YS, Pratsinis SE (1995) J Mater Sci 30:2803. doi:10.1007/BF00349647
35. Brinker CJ, Scherer GW (1990) Sol-gel science: the physics and chemistry of sol-gel processing. Academic Press, San Diego
36. MacLachlan MJ, Ginzburg M, Coombs N, Raju NP, Greedan JE, Ozin GA et al (2000) J Am Chem Soc 122:3878. doi:10.1021/ja992006y
37. Ziolo RF, Giannelis EP, Weinstein BA, O'Horo MP, Ganguli BN, Mehrotra V et al (1992) Science 257:219. doi:10.1126/science.257.5067.219